

Journal of Biomedical Optics

SPIEDigitalLibrary.org/jbo

Diffuse correlation spectroscopy with a fast Fourier transform-based software autocorrelator

Jing Dong
Renzhe Bi
Jun Hui Ho
Patricia S. P. Thong
Khee-Chee Soo
Kijoon Lee

Diffuse correlation spectroscopy with a fast Fourier transform-based software autocorrelator

Jing Dong,^a Renzhe Bi,^a Jun Hui Ho,^a Patricia S. P. Thong,^b Khee-Chee Soo,^b and Kijoon Lee^a

^aNanyang Technological University, Division of Bioengineering, School of Chemical and Biomedical Engineering, Singapore 637457, Singapore

^bNational Cancer Center Singapore, Division of Medical Sciences, Singapore 169610, Singapore

Abstract. Diffuse correlation spectroscopy (DCS) is an emerging noninvasive technique that probes the deep tissue blood flow, by using the time-averaged intensity autocorrelation function of the fluctuating diffuse reflectance signal. We present a fast Fourier transform (FFT)-based software autocorrelator that utilizes the graphical programming language LabVIEW (National Instruments) to complete data acquisition, recording, and processing tasks. The validation and evaluation experiments were conducted on an in-house flow phantom, human forearm, and photodynamic therapy (PDT) on mouse tumors under the acquisition rate of ~ 400 kHz. The software autocorrelator in general has certain advantages, such as flexibility in raw photon count data preprocessing and low cost. In addition to that, our FFT-based software autocorrelator offers smoother starting and ending plateaus when compared to a hardware correlator, which could directly benefit the fitting results without too much sacrifice in speed. We show that the blood flow index (BFI) obtained by using a software autocorrelator exhibits better linear behavior in a phantom control experiment when compared to a hardware one. The results indicate that an FFT-based software autocorrelator can be an alternative solution to the conventional hardware ones in DCS systems with considerable benefits. © 2012 Society of Photo-Optical Instrumentation Engineers (SPIE). [DOI: [10.1117/1.JBO.17.9.097004](https://doi.org/10.1117/1.JBO.17.9.097004)]

Keywords: correlators; Fourier transforms; multiple scattering; optical devices.

Paper 12152 received Mar. 5, 2012; revised manuscript received Jun. 24, 2012; accepted for publication Jul. 9, 2012; published online Sep. 14, 2012.

1 Introduction

Near-infrared diffuse correlation spectroscopy (DCS), also known as diffusing-wave spectroscopy (DWS), is established on the well-known spectral window in the near-infrared (NIR, 650 to 900 nm) range, wherein the relatively low biological tissue absorption enables deep penetration of light. It is an emerging technique for continuous noninvasive measurement of blood flow in biological tissues. In the last decade or so, DCS technology has been developed,^{1–3} extensively validated, and vigorously employed to noninvasive probe the blood flow information in deep tissue vasculature, such as brain,^{4–19} muscle,^{20–25} and breast.^{26,27} Compared to other blood flow measurement techniques, such as positron emission tomography (PET), single photon emission computed tomography (SPECT), and xenon-enhanced computed tomography (XeCT), DCS uses nonionizing radiation and needs no contrast agents. In contrast to dynamic susceptibility contrast magnetic resonance imaging (DSC-MRI) and arterial spin labeling MRI (ASL-MRI), it has no interference with commonly used medical devices, such as pacemaker and metal implants.²⁸ Therefore, it has also been applied to cancer therapy monitoring^{29–32} and bedside monitoring in clinical settings.³³

The typical setup of the DCS technique consists of a laser with long coherence length as the light source, a photon-counting avalanche photodiode (APD) or photomultiplier tube (PMT) as the detector, and a hardware autocorrelator. As one of the critical components, the autocorrelator computes the

autocorrelation function of the temporal fluctuation of the light intensity, which was subject to multiple scattering events before emerging from the investigated position on the sample surface. There are many commercial correlators available, such as the ones manufactured by ALV (Langen, F. R. Germany) and by Correlators.com (Bridge-water, New Jersey). To date, most published works have used these hardware autocorrelators for autocorrelation calculations,^{4,5,7,13,20,25,27,32,34} although a few of them had designed a multitau software correlator for dynamic light scattering and validated it by particle size measurement.^{35,36} The hardware correlators utilized multitau scheme, so they could be operated at a fast sampling speed thus offered real-time computing across a wide range of lag times from several nanoseconds to hours. However, they are relatively costly and not flexible since the fixed number of bits per channel results in a fixed lag time scale. Meanwhile, the software autocorrelator mentioned earlier was capable of measuring correlation functions over a time scale of ~ 5 μ s in real time,^{35,36} but it was not capable of recording the raw photon-count signal and therefore had limitations in terms of preprocessing of the raw photon count and post-measurement sanity checking.

In this paper, we demonstrate an alternative approach of DCS analysis using a software correlator based on fast Fourier transform (FFT). It is cost-effective, flexible, and can be easily implemented with other technologies. Furthermore, the ability of recording raw photon-count signal holds the potential of signal preprocessing before autocorrelation calculation, such as filtering out the noise caused by fluctuation of the laser source. It also provides room for investigating the methods other than autocorrelation to extract flow information from raw signals.

Address all correspondence to: Kijoon Lee, Nanyang Technological University, Division of Bioengineering, School of Chemical and Biomedical Engineering, N1.3-B3-12, 70 Nanyang Drive, Singapore 637457, Singapore. Tel: (65)6790-4702; Fax: (65)6791-1761; E-mail: kjlee@ntu.edu.sg

To achieve data acquisition, recording, and autocorrelation calculation, we used the graphical programming language LabVIEW (National Instruments), which is one of the most popular and powerful tools for signal acquisition and processing. The FFT, which is one of the most efficient algorithms known in the history of signal processing, was applied for autocorrelation calculation. The sampling rate of the system can reach up to ~ 400 kHz and thus enables the minimum lag time of ~ 2.5 μ s, which is significantly shorter than the decay constant (between tens to hundreds of microseconds) in DCS applications. Through comparison with a simulated hardware autocorrelator that works the same way as a hardware correlator (correlator.com) does, we evaluated the performance of the FFT-based software autocorrelator. For the purpose of validation, in-house flow phantom experiment, a human arm cuff occlusion experiment as well as a photodynamic therapy (PDT) response monitoring experiment were conducted.

This paper is organized as follows. In Sec. 2, we recall the theoretical background of DCS. In Sec. 3, a detailed description of our FFT-based software autocorrelator, as well as comparison with a simulated hardware autocorrelator are presented. The experimental setup for both phantom and *in vivo* experiments are described in Sec. 4, followed by an interpretation of the experimental results in Sec. 5. The concluding remarks are presented in Sec. 6.

2 Theoretical Background of DCS

The biological tissue can be characterized by its optical properties, such as the absorption coefficient μ_a and the reduced scattering coefficient μ'_s . When diffusing photons scatter from moving scatterers, they experience phase shifts and cause the speckle fluctuation at the detector side. The motion information below the tissue surface is carried in the electric field of diffuse light $E(\vec{r}, \tau)$ and can be extracted from the electric field autocorrelation function, which is defined as $G_1(\vec{r}, \tau) = \langle E(\vec{r}, t)E^*(\vec{r}, t + \tau) \rangle$. It has been shown that $G_1(\vec{r}, \tau)$ satisfies a correlation diffusion equation, i.e.,^{1,3,4,37}

$$\left[-\frac{1}{3\mu'_s} \nabla^2 + \mu_a + \frac{1}{3} \alpha \mu'_s k_0^2 \langle \Delta r^2(\tau) \rangle \right] G_1(\vec{r}, \tau) = S(\vec{r}), \quad (1)$$

where k_0 is the wavenumber of the light in a medium, α is the fraction of photon scattering events from moving scatterers out of total scatterers, and $\langle \Delta r^2(\tau) \rangle$ represents the mean square displacement of the moving scatterers, and is commonly described using two different models, namely the Brownian motion and random flow model in biological tissues. The Brownian motion model considers the motion of scatterers as diffusive motion and $\langle \Delta r^2(\tau) \rangle = 6D_B\tau$,^{38,39} where D_B is the effective diffusion coefficient of the scatterers. Meanwhile, the random flow model assumes the random ballistic motion of scatterers and $\langle \Delta r^2(\tau) \rangle = \langle V^2 \rangle \tau^2$ (Refs. 40 and 41), where $\langle V^2 \rangle$ represents the mean square velocity of the scatterers. Experimentally, the diffuse light electric field autocorrelation function is usually derived from the measured normalized intensity autocorrelation $g_2(\vec{r}, \tau) = \langle I(\vec{r}, t)I(\vec{r}, t + \tau) \rangle / \langle I \rangle^2$ by using the Siegert relation:^{4,13,42}

$$g_2(\vec{r}, \tau) = 1 + \beta \frac{|G_1(\vec{r}, \tau)|^2}{\langle I(\vec{r}, t) \rangle^2}, \quad (2)$$

where $I(\vec{r}, t)$ is the detected diffusing light intensity at position r and time t , the angle bracket $\langle \dots \rangle$ denotes an ensemble

average, and β here is a numerical factor related to the detector geometry, number of detected speckles, and other experimental parameters. The assumption for applying the Siegert relation to obtain the electric field autocorrelation function is that the system is ergodic, which means the time average is equal to the ensemble average. The analytic solution of the correlation diffusion equation for a point light source upon a semi-infinite medium is^{4,43}

$$G_1(\rho, \tau) = \frac{3\mu'_s}{4\pi} \left(\frac{e^{-k_D r_1}}{r_1} - \frac{e^{-k_D r_2}}{r_2} \right), \quad (3)$$

where $k_D = \sqrt{3\mu'_s \mu_a + 6\mu'_s k_0^2 \alpha D_B \tau}$, $r_1 = \sqrt{\rho^2 + z_0^2}$ ($r_2 = \sqrt{\rho^2 + (z_0 + 2z_b)^2}$) are the distance between source (image source) and detector, respectively, in which ρ is the source detector separation, $z_0 = 1/\mu'_s$, $z_b = 2(1 - R_{\text{eff}})/3\mu'_s(1 + R_{\text{eff}})$ and R_{eff} represents the effective reflectance. Although physically the motion of blood cells may be considered as random flow, the Brownian motion model showed better fitting in the majority of cases, ranging from brain^{4,7-9,11-14,17} to muscle^{20,23} and tumor models.^{27,29,30,32} Therefore, the measurements of $G_1(\vec{r}, \tau)$ can be fitted to yield a blood flow index (BFI = αD_B) to parameterize the relative blood flow.

The BFI and β were obtained by minimizing the difference between the analytical model of the autocorrelation in the reflectance geometry $g_{1,m}(\vec{r}, \tau)$ and the measured autocorrelation function $g_{1,\text{exp}}(\vec{r}, \tau)$. The optimization of the objective function $\chi^2 = \sum [g_{1,m}(\vec{r}, \tau) - g_{1,\text{exp}}(\vec{r}, \tau)]^2$ was done by using Matlab (Mathwork, Inc.). The relative blood flow (rBF), which is the deviation of BFI with respect to the baseline, is reported in the unit of percent.

3 Data Acquisition and Processing

The DCS system consisted of a continuous-wave laser with a long coherence length (>10 m) operating at 785 nm (DL785-100-S, ~ 100 mW, CrystaLaser, Reno, Nevada, USA) as the source and a photon-counting APD (SPCM-AQRH-13-FC, Perkin-Elmer, Vudreuil-Dorion, Quebec, Canada), whose output was a stream of transistor-transistor logic (TTL) pulses, as the detector. The light from the source was coupled to a multi-mode optical fiber (200- μ m diameter) and contacted with a sample surface. The detecting fiber was single-mode operated at 785 nm (9- μ m diameter), which was located several centimeters away from the source fiber and fed to the APD. The TTL output generated by the APD was connected to the 32-bit, eight-input channel counter/timer board with the maximum input rate of 80 MHz (PCI-6602, National Instruments). The counter/timer board was connected to a PC (CPU: Intel Core 2 Duo, RAM: 3-Gbyte) through a shielded I/O connector block for DAQ devices (SCB-68, National Instruments).

3.1 Data Acquisition Principle

The performance was controlled by LabVIEW (National Instruments), which is one of the most popular and powerful program tools and suitable for interactive data acquisition and signal processing. The TTL output of the detector was counted over sampling time τ by the counter/timer board. The PCI-6602 has a timebase of 80 MHz, which means the fastest input pulses that can be counted are 12.5 ns (1/80,000,000 s) apart. The PCI-6602 is the 32-bit counter and can count up to 4,294,967,295 ($2^{32} - 1$) before it rolls over. The counter can count the events

continuously and store the data in the buffer. Due to the limitation of buffer size, time resolution of anything less than $2 \mu\text{s}$ would fill up the buffer in less than 1 s. For the purpose of stable data acquisition, we conducted experiments using $2.5 \mu\text{s}$. In the data acquisition program, we applied “queue” structure to link the “producer” loop and the “consumer” loop, which were in charge of reading photon counts and writing results to a file, respectively. By using this kind of structure, the two loops were able to work in parallel so that a faster speed can be achieved. Simultaneously, another LabVIEW program detected the latest written photon-counting file and calculated the autocorrelation function by FFT algorithm. The result was then displayed and saved to a specified folder. Running on our current system, one core of CPU was fully occupied to acquire the data, while the other core was used for the autocorrelation calculation.

3.2 Data Processing

In this section, the working principle of the hardware correlator board will be briefly described, based on the instruction manual of a most commonly used commercial product (Flex99R-12) from Correlator.com. The algorithm behind the hardware correlator will be simulated by the software approach, and its performance will be compared against our new FFT-based approach in a later section.

3.2.1 Simulating hardware autocorrelator board

Inside the hardware autocorrelator board. The typical hardware correlators such as the ones manufactured by ALV and Correlator.com are based on a multitaup scheme, and have a multiple tier structure which contains a certain amount of registers as shown in Fig. 1. If we take the one from Correlator.com for instance, the first tier has 32 registers, and higher tiers have 16 registers each. The incoming photon count starts filling up the registers in the first tier from the left with a given delay time T_0 (typically 160 ns). When it reaches the right end, the second tier fills up from the left at a twice as slow rate, since the sum of two register values in the right end of the first tier constructs the first register value of the second tier. Likewise, the first register value of n th tier is constructed by sum of the last two register values in $(n-1)$ th tier, which means the registers of n 'th tier is updated every $2^{n-1}T_0$. The hardware correlator can have upto 31 tiers, which means there are $512 [(1 \times 32) + (30 \times 16)]$ registers with 512 different delay times. However, registers at the 31st tier updates every

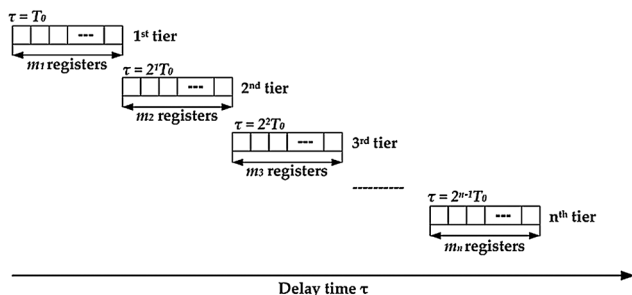


Fig. 1 The diagram of hardware autocorrelator inner structure, with several tiers of registers where the delay times are the power of two times of initial delay time T_0 .

$2^{30}T_0$, which is too long with a practical T_0 value of ~ 100 ns, so later tiers are hardly used in practice.

For each shift that occurs in the register, the unnormalized intensity autocorrelation coefficient for the i th register, $G_2(t_i)$, is calculated as the average value of $n_i \cdot n_0$, where n_i indicates the photon count in the i th register, n_0 is the photon count at zero delay time with the same bin width as the i th register, and t_i is the delay time between n_i and n_0 .²⁸ The delay time t_i is calculated as the summation of all the bin widths on the left of the i th register. With a few hundred register channels (512 channels for a 31 tier system, for example), a delay time that ranges from hundred of nanoseconds to minutes can be achieved, greatly reducing the computational load compared to the linear autocorrelator.

Software implementation. The above mentioned hardware correlator algorithm is implemented in Matlab, in order to examine its behavior with a known input signal, generated either by simulation or experiment. The number of tiers, N , was given as a variable (normally set at around 10), and a cell array variable with a size of $16(N+1)$ [32 for 1st tier, and $16(N-1)$ afterwards] was allocated for register channels. The Matlab script initiates a loop, where the register channels in the first tier shifts to the right by one register per iteration and a new datum is read in the left-most register. When the iteration number reaches 2^{n+1} , registers in n 'th tier become shifted to the right by one register, after which a new value [the sum of two register values at the end of $(n-1)$ 'th tier] is assigned to the left-most register in n 'th tier. Figure 2 shows a snapshot of the register profile in different tiers, where the register values are represented in a logarithmic scale to better visualize the wide-range of the values.

When the register fully fills up, the autocorrelation coefficient between i th register and the 0th register (with the same bin width, as described previously in the hardware correlator section) is calculated. The autocorrelation curve for whole register is calculated for each shift event in the last tier, and they are averaged over hundreds of trials before being plotted.

3.2.2 FFT-based software autocorrelator

The unnormalized intensity autocorrelation, represented as $G_2(\tau) = \langle I(t)I(t+\tau) \rangle$, resembles the convolution operation, except that in the convolution calculation, the second term being multiplied has to be the time-reversal of the original function $I(t)$, namely $I(-t)$. Therefore, the same autocorrelation can be obtained by convolution between two functions $I(t)$ and $I(-t)$. Then, by the convolution theorem, one can obtain the autocorrelation function based on the Fourier transform as follows:

$$\begin{aligned} G_2(\tau) &= (I(t) * I(-t))(\tau) = F^{-1}[F\{I(t)\}F\{I(-t)\}] \\ &= F^{-1}\{\tilde{I}(v)\tilde{I}(v^*)\} = F^{-1}\{|\tilde{I}(v)|^2\}, \end{aligned} \quad (4)$$

where F and F^{-1} refer to forward and inverse Fourier transform, respectively, and $\tilde{I}(v)$ is the Fourier transform of $I(t)$. Note that the last equality of Eq. (4) is also called Wiener-Khinchin theorem and real valued $I(t)$ always results in real values of G_2 .

Since the Fourier transform can be very efficiently implemented by the fast Fourier transform (FFT), one can obtain the linear autocorrelation function in a very fast and stable manner using above equation.

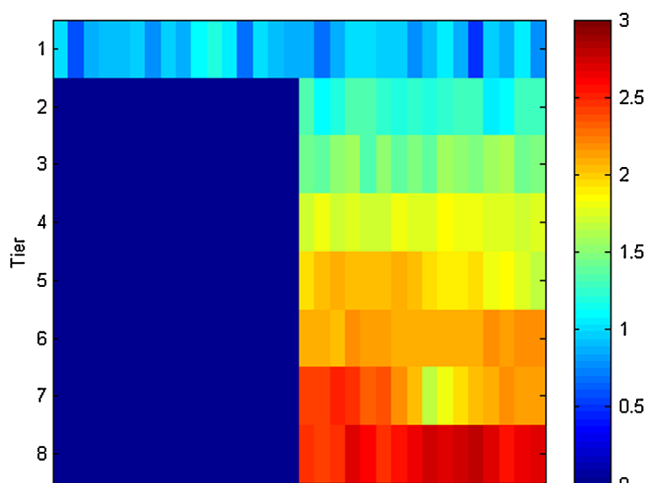


Fig. 2 A snapshot of the registers of simulated hardware correlator. Color represents the logarithm of the photon count in each register. Ignore the blue portion on the left where there are no registers.

Figure 3 shows the comparison between the two normalized intensity autocorrelation $g_2(\tau)$ calculations, one from the multitau approach simulating the hardware correlator board, and the other from the FFT-based linear approach. The data used in Fig. 3(a) was from a flow phantom experiment, acquired by the NI counter board (PCI-6602) at the sampling rate of 400 kHz. For the FFT-based approach, the data size used was about 4×10^5 , covering about 1 s. For the hardware simulating approach, the delay time was only calculated upto about 30 ms due to the small number of tiers (10 tiers were used), but it was averaged over 500 autocorrelation calculations, and the total length of data used is about the same. The FFT-based calculation always ends up showing a spike near the highest delay time, but that is due to the cyclic nature of the FFT-based result, and our visualization in Fig. 3 only shows the first half, thereby removing the unwanted peak. Both of them show a nice convergence to the value of 1 for long delay times, and they nicely overlap with each other. For the experimental data in general, we were able to observe a trend that the hardware (multitau) algorithm

tends to show higher fluctuation for small delay times, whereas the FFT-based algorithm always show the smoothest behavior for small delay times due to its single-tau calculation.

The comparison was also performed using simulated data based on a Markov chain with a Gaussian noise, and the result was always overlapping unless the average count value of the data was too low. When the average was low, we were able to regain the equivalence between the two methods by binning the data, thereby increasing the average photon count value. Typical autocorrelation curves for simulated data are shown in Fig. 3(b).

4 Experiment

4.1 In-House Flow Phantom Experiment

Phantom, which is the tissue-simulating object to mimic the properties of human or animal tissues, has played an important role in the evolution of diagnostic systems, and most physical therapeutic interventions. It can be used for the purposes of initial testing of system design, optimizing signal to noise ratio (SNR) in existing system, and so on.⁴⁴ In order to validate and assess the ability of our system, a flow phantom was built as shown in Fig. 4.

The phantom making procedure can be found elsewhere.⁴⁵ Briefly, RTV 12A was the base compound, RTV 12C (Momentive Performance Materials) was the curing agent, while carbon black and TiO_2 were mixed to adjust the absorption coefficient and scattering coefficient, respectively. The optical properties of the solid flow phantom were $\mu'_s = 8 \text{ cm}^{-1}$ and $\mu_a = 0.03 \text{ cm}^{-1}$ (measured by OxiplexTS, ISSInc, at 830 nm), which satisfied the $\mu'_s \gg \mu_a$ criterion, and the photon diffusion equation remains valid.

The schematic of the DCS experimental setup is shown in Fig. 5. The Lipofundin N 20% (B.BraunMelsungen AG, Germany) with a concentration of 0.6% was pumped through the cylindrical tube, with flow speeds of 0 ml/s, 0.05 ml/s, 0.125 ml/s, 0.2 ml/s, and 0.325 ml/s. The source-detector pair was centered over the solid phantom surface at a distance of 1 cm from the flow tube surface. Reflection geometry was adopted in which incident light was injected into the phantom

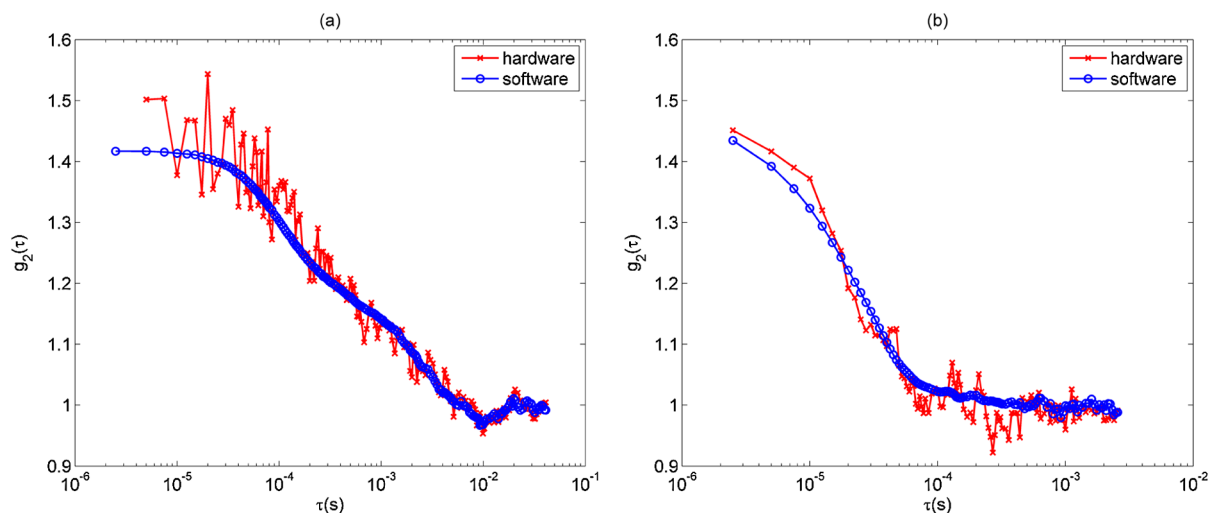


Fig. 3 Comparison between hardware and software autocorrelation calculations. (a) Autocorrelation calculated from a typical flow phantom data. (b) Autocorrelation calculated from a simulated data. Hardware-simulating algorithm (red squares) was implemented under the assumption of a 10-tier register, averaged over 500 different autocorrelations. The sampling rate was 400 kHz.

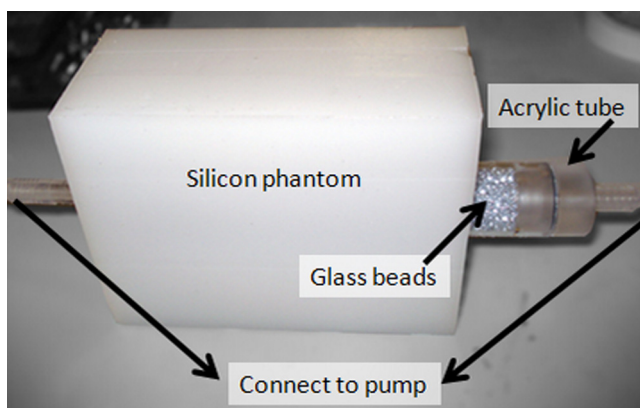


Fig. 4 The in-house silicon flow phantom, in which an acrylic cylindrical tube was embedded to mimic the blood vessel. The tube was filled up with glass beads with a diameter of 3 mm in order to make random flow directions.

by the source fiber and detected 3.0 cm away along with the cylindrical tube direction.

4.2 In Vivo Cuff Occlusion Experiment on a Human Arm

After the flow phantom experiment, we conducted the validation study on a human subject. The *in vivo* cuff occlusion experiment was done on the arm of a 28 year-old healthy male subject. In order to vary the blood flow speed, a cuff on the subject's upper

arm was constricted for 15 s for temporary arterial occlusion. The source-detector separation was 1.5 cm and the probes were located on the forearm. The cuff inflation pressure was 200 mmHg.

4.3 Photodynamic Therapy Response Monitoring

Besides the flow phantom and *in vivo* human arm cuff occlusion experiments, we also applied our instrument to a lab-based PDT experiment for evaluation. Since the antivascular effects of PDT is a key indicator of tissue response to treatment,²⁹ we aim to provide instantaneous hemodynamic feedback on treatment response. The *in vivo* PDT experiment was approved by the Institutional Animal Care and Use Committee of Singapore Health Services Pte Ltd and carried out at the National Cancer Centre Singapore. A Balb/c mouse bearing xenograft tumors on the flanks was used as an animal model. The mouse received chlorin e6 (Ce6) as the photosensitizer at a dose of 5 mg/kg. Approximately 4 h after injection, the tumors were irradiated with laser light. The irradiation lasted 2450 s, consisting of alternating 250-s light exposures and 300-s dark intervals. The treatment light for PDT was delivered by a 665-nm medical-grade laser (Biolitec, Germany). The light dose used was 100 J/cm², delivered at a rate of 80 mW/cm² via an optical fiber. The treatment light was expanded to a 2.5-cm diameter on the tumor surface. Our DCS measurement was carried out before and immediately after each exposure, as well as at 25 and 50 min after the last treatment. Source-detector separation was 1 cm, which fitted the size of the tumors.

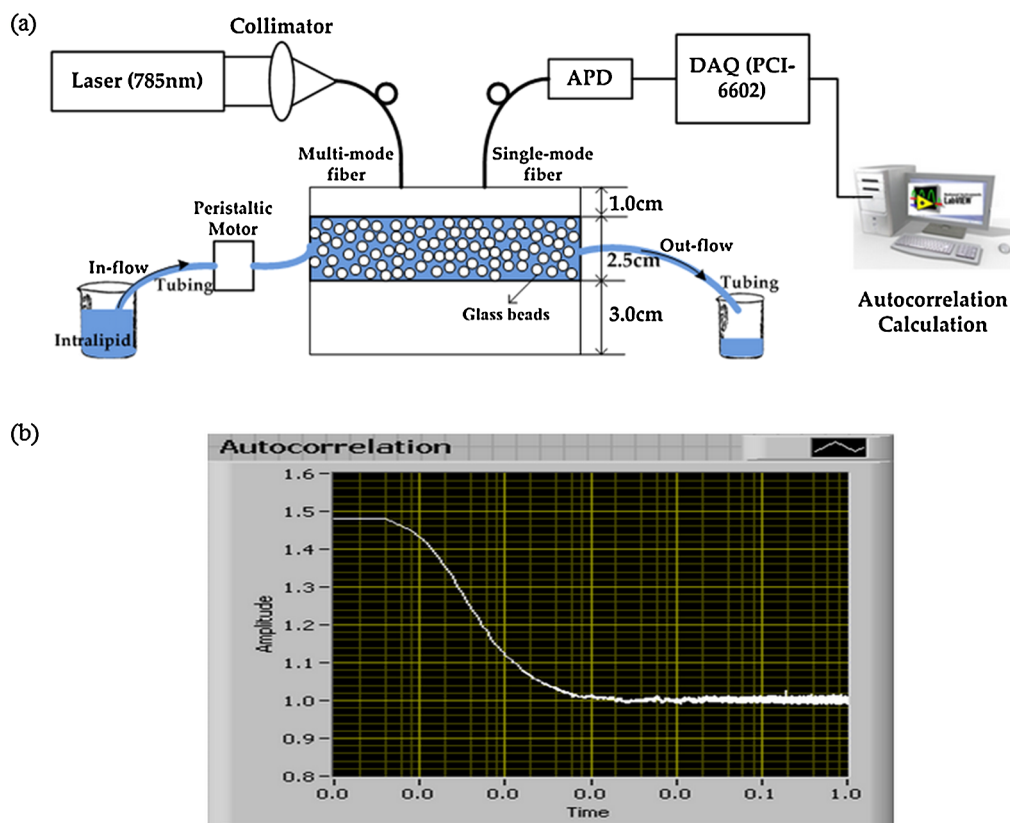


Fig. 5 (a) Schematic of the DCS experimental setup using in-house flow phantom. (b) Screen shot of the LabVIEW interface of the FFT-based autocorrelation calculation.

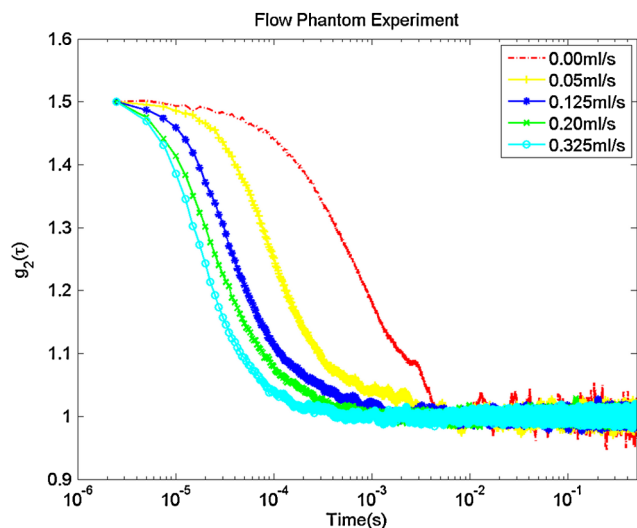


Fig. 6 Autocorrelation curves of the phantom with varied speed of flow (0 ml/s, 0.05 ml/s, 0.125 ml/s, 0.2 ml/s, and 0.325 ml/s) as a function of delay time, τ .

5 Results and Discussion

5.1 In-House Flow Phantom Experiment

Figure 6 shows the normalized intensity autocorrelation functions in a semilogarithm plot with varying flow speed. It can be observed that the normalized intensity autocorrelation function $g_2(\tau)$ showed an initial constant plateau, but decayed exponentially with increasing delay time. As speed increased, the decay rate of the autocorrelation curve increased. If we recall the definition of autocorrelation, the finite data length will always cause the copy of the data shift out of the data window, thus eventually the autocorrelation function will go down to zero naturally. However, by employing an FFT, one can actually get the cyclic autocorrelation, thus it avoids the edge effect caused by data finiteness and offers a faster calculating speed. Ideally, the zero flow (0 ml/s) was not supposed to show any decay, but we observed a decay that is mainly attributed to the intrinsic fluctuation of the laser source and the room temperature Brownian motion of the Lipofund in remaining in the tubing. The autocorrelation function calculating speed was less than 20 milliseconds for 800,000 data points with the type of double-precision integer, which is faster than the data writing speed (new file generating speed) and enables the display of the autocorrelation curve in almost real-time. We note from the autocorrelation curves, that increasing the flow causes the plateau region of the curves to be shorter and makes it difficult to determine the β value. Therefore, it might cause inaccuracy in measuring high flow, but one can obtain stable plateaus for most of the relevant flow ranges *in vivo*.

Since FFT-based autocorrelation calculation provided smoother starting and ending plateaus, it was obviously able to improve curve fitting. For better comparison between the Brownian motion and random flow model, we performed curve fitting by using both models. The Levenberg-Marquardt algorithm was applied in Matlab (Mathwork, Inc., *nlinfit* function). As indicated by Fig. 7, which was the autocorrelation function of the flow with speed of 0.325 ml/s, the Brownian motion model fit the experimental data better than the random flow model did. This result also suggested that our

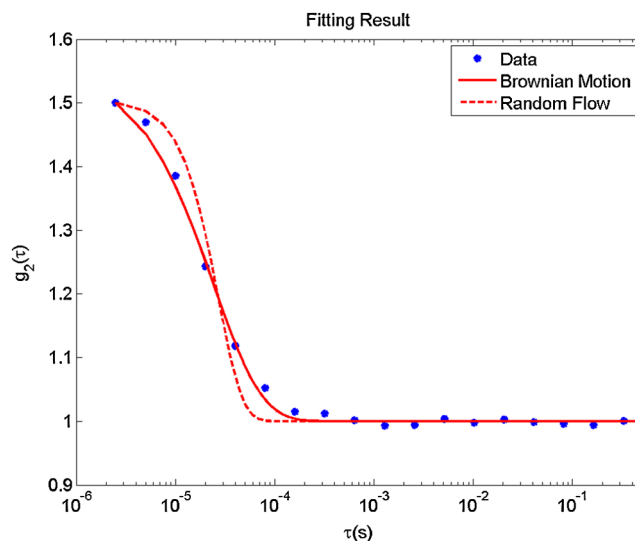


Fig. 7 Comparison between Brownian motion and the random flow model. The autocorrelation function was calculated from the flow phantom data with a speed of 0.325 ml/s. The entire autocorrelation data was sampled and shown as dots.

self-designed phantom is able to mimic the capillary flow of the human body. Therefore, we conducted curve fitting by using the Brownian motion model, and the blood flow index ($BFI = \alpha D_B$) was obtained. The fitting result in general depends highly on the methods of data sampling. In order to obtain better fitting with a uniform weightage in the logarithmic time scale, we sampled the entire autocorrelation function equally on 2-base logarithm scale as shown in Fig. 7. This subsampling helps with faster fitting speed without compromising its accuracy.

In order to compare the goodness of fitting of the FFT-based software autocorrelator with that of the simulated hardware autocorrelator, we calculated a 95% confidence interval of fitted parameters by using an *nlparci* function in Matlab (Mathwork, Inc.). As shown in Fig. 8, by using a speed of 0 ml/s as a base, relative αD_B and $\sqrt{\alpha \langle V^2 \rangle}$ with their standard deviations at different flow speeds were calculated in both software and hardware cases. It can be found that in either the Brownian motion or random flow model, the standard deviations of the fitted parameter in FFT-based software autocorrelator were always smaller than in the hardware one. Concurrently, in the same autocorrelator, the parameter fitted for the Brownian motion had a smaller standard deviation than that for the random flow model and it also can be observed from individual fitting as shown in Fig. 7. Moreover, we performed a linear regression of the relative αD_B and $\sqrt{\alpha \langle V^2 \rangle}$. It showed higher linearity to flow speed in the software autocorrelator case than in the hardware one. In addition, as mentioned previously, the autocorrelation calculating speed is faster than the data writing speed, our instrument holds the potential to make full use of this time to accomplish data fitting and provide the rBF values in real-time.

5.2 In Vivo Human Arm Cuff Occlusion Experiment

Figure 9(a) shows the normalized intensity autocorrelation function $g_2(\tau)$ of three stages of the *in vivo* cuff occlusion experiment, namely baseline, cuff inflation, and cuff deflation.

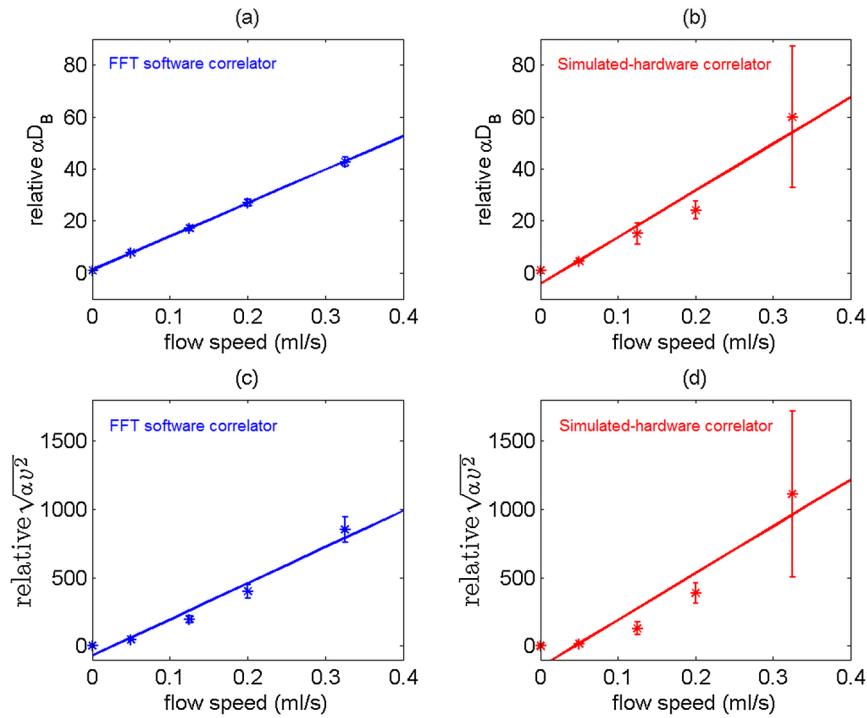


Fig. 8 Linearity test of relative BFI (either αD_B or $\sqrt{\alpha(V^2)}$) versus flow speed. (a) and (c) are obtained using a software autocorrelator (shown in blue), while (b) and (d) are obtained using a hardware autocorrelator (shown in red). All RBFs are normalized to the BFI value at zero flow.

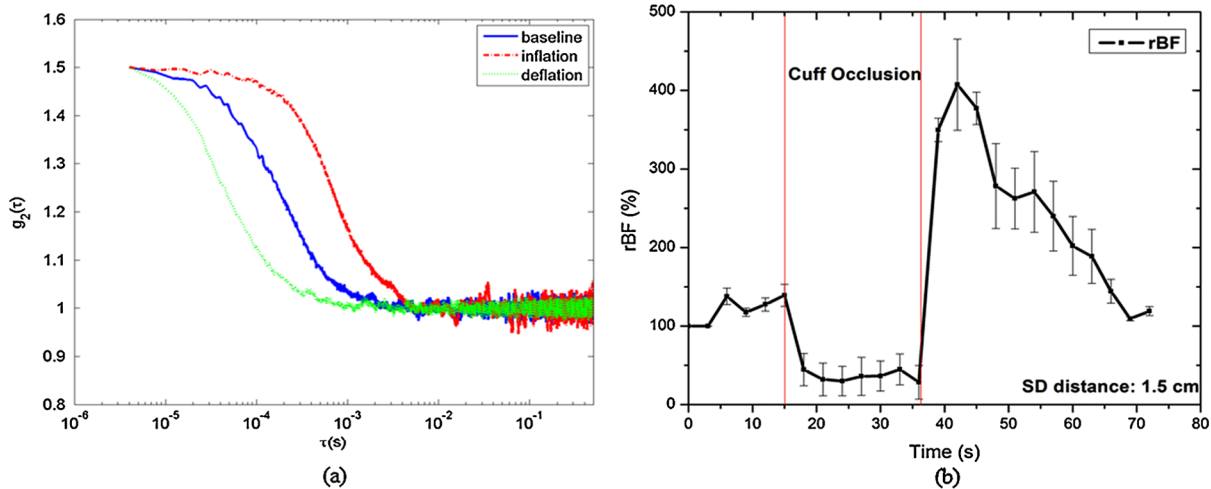


Fig. 9 (a) Autocorrelation functions of cuff occlusion stages, namely baseline (blue solid line), cuff inflation (red dash-dot line), and cuff deflation (green dashed line). (b) Representative time response of relative blood flow (rBF) during cuff occlusion experiment, including baseline recording, cuff inflation (cuff occlusion period on the figure), and cuff deflation stages.

The baseline curve was averaged over the first 15 s, the inflation curve was averaged over the 15th to 35th seconds, while the deflation curve was the average of only the 35th to 45th seconds. The decay rate of $g_2(\tau)$ shows significant change. Figure 9(b) reveals rBF, which was obtained by fitting $g_2(\tau)$ to the solution of the photon diffusion correlation equation. For the first 15 s, the blood flow was constant as no constriction was applied. Once the constriction was applied to the cuff, the blood flow dropped down sharply and when constriction was released, the blood flow immediately showed an overshoot followed by a slow decrease to the baseline due to homeostasis.

5.3 PDT Monitoring Experiment

We plotted the DCS monitoring result during the PDT treatment in Fig. 10. The color bars in the figure represent PDT light intervals.

The mean tumor rBF decreased by $\sim 50\%$ immediately after the whole PDT, and decreased to $\sim 45\%$ of the baseline 60 min after treatment. During each PDT dark interval, blood flow changes showed minor fluctuations. They indicate impermanent vessel occlusion during PDT light intervals. These temporary vessel occlusions can be reversible, and it allows flow recovery during the dark intervals. A similar trend was observed

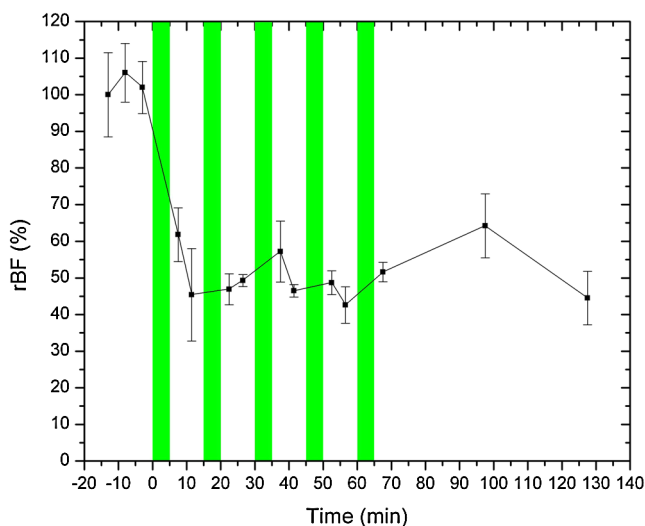


Fig. 10 The time behavior of relative blood flow (rBF) before, during, and after PDT treatment. The color bars represent the light exposures during treatment; there was no data recorded during light exposure intervals.

using laser Doppler measurements, although different animal models were used in each case.⁴⁶ However, the results after 60 min suggest that permanent vessel occlusion had occurred due to PDT.

6 Conclusion

In this paper, we have demonstrated an implementation of DCS system with an FFT-based software autocorrelator. The operation of the system was controlled by LabVIEW. The software autocorrelator has undergone the validation and assessment by an in-house flow phantom experiment, *in vivo* cuff occlusion experiment on a human arm, as well as a PDT response monitoring experiment. It is easy to operate and relatively cost-effective. Besides, though the data sampling speed is moderate, the minimum lag time is much shorter than the decay constant, thus the extraction of the desired parameter is still valid. Furthermore, smoother starting and ending plateaus improve the accuracy in data fitting, and hence in the blood flow index. In addition, the system still holds the potential of being a real-time flow indicator and can be used for future DCS systems in research and clinical settings.

Acknowledgments

This work is supported by the Singapore Ministry of Education under the Academic Research Fund Tier1 Grant RG37/07 and partially supported by a SingHealth Foundation Grant (SHF/FG385P/2008). The PDT experiment was performed in collaboration with the National Cancer Centre Singapore. We thank Dr. Hamid Dehghani for useful discussions, and Mr. Bobby Chow and Mr. Peng Zu for helpful technical assistance. We also thank Ms. Hui Jin Toh and Mr. Chuan-Sia Tee of the National Cancer Centre Singapore for assistance with the PDT experiments. Support from Ms. Melda and Dr. Yongjin are also gratefully acknowledged.

References

- D. A. Boas, L. E. Campbell, and A. G. Yodh, "Scattering and imaging with diffusing temporal field correlations," *Phys. Rev. Lett.* **75**(9), 1855–1858 (1995).
- D. A. Boas et al., "Diffusion of temporal field correlation with selected applications," *Biophys. J.* **70**(2), WP306–WP306 (1996).
- D. A. Boas and A. G. Yodh, "Spatially varying dynamical properties of turbid media probed with diffusing temporal light correlation," *J. Opt. Soc. Am. A* **14**(1), 192–215 (1997).
- C. Cheung et al., "In vivo cerebrovascular measurement combining diffuse near-infrared absorption and correlation spectroscopies," *Phys. Med. Biol.* **46**(8), 2053–2065 (2001).
- J. P. Culver et al., "Diffuse optical tomography of cerebral blood flow, oxygenation, and metabolism in rat during focal ischemia," *J. Cereb. Blood Flow Metab.* **23**(8), 911–924 (2003).
- J. P. Culver et al., "Diffuse optical measurement of hemoglobin and cerebral blood flow in rat brain during hypercapnia, hypoxia and cardiac arrest," *Adv. Exp. Med. Biol.* **510**, 293–297 (2003).
- T. Durduran et al., "Diffuse optical measurement of blood flow, blood oxygenation, and metabolism in a human brain during sensorimotor cortex activation," *Opt. Lett.* **29**(15), 1766–1768 (2004).
- J. Li et al., "Noninvasive detection of functional brain activity with near-infrared diffusing-wave spectroscopy," *J. Biomed. Opt.* **10**(4), 044002 (2005).
- C. Zhou et al., "Diffuse optical correlation tomography of cerebral blood flow during cortical spreading depression in rat brain," *Opt. Express* **14**(3), 1125–1144 (2006).
- M. N. Kim et al., "Validation of diffuse correlation spectroscopy against xenon CTCBF in humans after traumatic brain injury or subarachnoid hemorrhage," in *Neurocritical Care Society Annual Meeting*, Humana Press Inc, Miami, FL (2008).
- J. Li et al., "Transient functional blood flow change in the human brain measured noninvasively by diffusing-wave spectroscopy," *Opt. Lett.* **33**(19), 2233–2235 (2008).
- E. M. Buckley et al., "Cerebral hemodynamics in preterm infants during positional intervention measured with diffuse correlation spectroscopy and transcranial Doppler ultrasound," *Opt. Express* **17**(15), 12571–12581 (2009).
- T. Durduran et al., "Transcranial optical monitoring of cerebrovascular hemodynamics in acute stroke patients," *Opt. Express* **17**(5), 3884–3902 (2009).
- C. Zhou et al., "Diffuse optical monitoring of hemodynamic changes in piglet brain with closed head injury," *J. Biomed. Opt.* **14**(3), 034015 (2009).
- S. A. Carp, G. P. Dai, and D. A. Boas, "Validation of diffuse correlation spectroscopy measurements of rodent cerebral blood flow with simultaneous arterial spin labeling MRI; towards MRI-optical continuous cerebral metabolic monitoring," *Biomed. Opt. Express* **1**(2), 553–565 (2010).
- M. Kim et al., "Noninvasive measurement of cerebral blood flow and blood oxygenation using near-infrared and diffuse correlation spectroscopies in critically brain-injured adults," *Neurocrit. Care* **12**(2), 173–180 (2010).
- N. Roche-Labarbe et al., "Noninvasive optical measures of CBV, StO₂, CBF index, and rCMRO₂ in human premature neonates' brains in the first six weeks of life," *Human Brain Mapp.* **31**(3), 341–352 (2010).
- P. Zirak et al., "Effects of acetazolamide on the micro- and macrovascular cerebral hemodynamics: a diffuse optical and transcranial doppler ultrasound study," *Biomed. Opt. Express* **1**(5), 1443–1459 (2010).
- Y. Shang et al., "Diffuse optical monitoring of repeated cerebral ischemia in mice," *Opt. Express* **19**(21), 20301–20315 (2011).
- G. Yu et al., "Time-dependent blood flow and oxygenation in human skeletal muscles measured with noninvasive near-infrared diffuse optical spectroscopies," *J. Biomed. Opt.* **10**(2), 024027 (2005).
- G. Yu et al., "Validation of diffuse correlation spectroscopy for muscle blood flow with concurrent arterial spin labeled perfusion MRI," *Opt. Express* **15**(3), 1064–1075 (2007).
- M. Belau et al., "Noninvasive observation of skeletal muscle contraction using near-infrared time-resolved reflectance and diffusing-wave spectroscopy," *J. Biomed. Opt.* **15**(5), 057007 (2010).
- Y. Shang, T. B. Symons, and T. Durduran, "Effects of muscle fiber motion on diffuse correlation spectroscopy blood flow measurements during exercise," *Biomed. Opt. Express* **1**(2), 500–511 (2010).

24. G. Yu et al., "Intraoperative evaluation of revascularization effect on ischemic muscle hemodynamics using near-infrared diffuse optical spectroscopies," *J. Biomed. Opt.* **16**(2), 027004 (2011).
25. N. Munk et al., "Noninvasively measuring the hemodynamic effects of massage on skeletal muscle: a novel hybrid near-infrared diffuse optical instrument," *J. Bodywork Movement Therap.* **16**(1), 22–28 (2012).
26. T. Durduran et al., "Diffuse optical measurement of blood flow in breast tumors," *Opt. Lett.* **30**(21), 2915–2917 (2005).
27. C. Zhou et al., "Diffuse optical monitoring of blood flow and oxygenation in human breast cancer during early stages of neoadjuvant chemotherapy," *J. Biomed. Opt.* **12**(5), 051903 (2007).
28. D. A. Boas, C. Pitris, and N. Ramanujam, *Handbook of Biomedical Optics*, CRC Press, Boca Raton (2011).
29. G. Yu et al., "Noninvasive monitoring of murine tumor blood flow during and after photodynamic therapy provides early assessment of therapeutic efficacy," *Clin. Cancer Res.* **11**(9), 3543–3552 (2005).
30. U. Sunar et al., "Noninvasive diffuse optical measurement of blood flow and blood oxygenation for monitoring radiation therapy in patients with head and neck tumors: a pilot study," *J. Biomed. Opt.* **11**(6), 064021 (2006).
31. G. Yu et al., "Real-time in situ monitoring of human prostate photodynamic therapy with diffuse light," *Photochem. Photobiol.* **82**(5), 1279–1284 (2006).
32. U. Sunar et al., "Hemodynamic responses to antivascular therapy and ionizing radiation assessed by diffuse optical spectroscopies," *Opt. Express* **15**(23), 15507–15516 (2007).
33. T. Durduran, "Diffuse optical monitors for bed-side monitoring of cerebral hemodynamics at the neuro-intensive care unit," in *IEEE Leos Annual Meeting Conf. Proc.*, pp. 270–271, IEEE, Belek-Antalya, Turkey (2009).
34. Y. Shang et al., "Portable optical tissue flow oximeter based on diffuse correlation spectroscopy," *Opt. Lett.* **34**(22), 3556–3558 (2009).
35. D. Magatti and F. Ferri, "Fast multi-tau real-time software correlator for dynamic light scattering," *Appl. Opt.* **40**(24), 4011–4021 (2001).
36. D. Magatti and F. Ferri, "25 ns software correlator for photon and fluorescence correlation spectroscopy," *Rev. Sci. Instrum.* **74**(2), 1135–1144 (2003).
37. M. Heckmeier et al., "Imaging of dynamic heterogeneities in multiple-scattering media," *J. Opt. Soc. Am. A* **14**(1), 185–191 (1997).
38. G. Maret and P. E. Wolf, "Multiple light scattering from disordered media. The effect of brownian motion of scatterers," *Zeitschrift für Physik B Condens. Matter* **65**(4), 409–413 (1987).
39. D. J. Pine et al., "Diffusing wave spectroscopy," *Phys. Rev. Lett.* **60**(12), 1134 (1988).
40. R. Nossal, S. H. Chen, and C. C. Lai, "Use of laser scattering for quantitative determinations of bacterial motility," *Opt. Commun.* **4**(1), 35–39 (1971).
41. R. Bonner and R. Nossal, "Model for laser Doppler measurements of blood flow in tissue," *Appl. Opt.* **20**(12), 2097–2107 (1981).
42. T. Dorfmueller, B. J. Berne, and R. Pecora, *Dynamic Light Scattering*, John Wiley and Sons Ltd., Baffins Lane (1976).
43. D. A. Boas, "Diffuse photon probes of structural and dynamical properties of turbid media theory and biomedical applications," Ph.D. thesis, University of Pennsylvania (1996).
44. B. W. Pogue and M. S. Patterson, "Review of tissue simulating phantoms for optical spectroscopy, imaging and dosimetry," *J. Biomed. Opt.* **11**(4), 041102 (2006).
45. R. Choe, "Diffuse optical tomography and spectroscopy of breast cancer and fetal brain," Ph.D. Thesis, University of Pennsylvania (2005).
46. B. W. Pogue et al., "Analysis of the heterogeneity of pO₂ dynamics during photodynamic therapy with verteporfin," *Photochem. Photobiol.* **74**(5), 700–706 (2001).